ATLAS soft tau reconstruction performance in the mSUGRA stau coannihilation region

Ola Kristoffer Øye, Anna Lipniacka

Department of Physics and Technology, University of Bergen, Norway

Abstract

We study the performance of the tau reconstruction algorithms tauRec and tau1P3P on simulated ATLAS data. We focus primarily on soft taus, an important signature of several models of new physics observable at the LHC. Optimisation of soft tau reconstruction is investigated, and the obtained performance is compared for the two algorithms. Some observations concerning tau decay kinematics in the generators Herwig and Pythia are documented. We use both algorithms to reconstruct the invariant mass of the tau pairs from the cascade decay $\chi_2^0 \to \tilde{\tau} + \tau; \tilde{\tau} \to \tau + \chi_1^0$ in the mSUGRA stau coannihilation region. The results are compared with generator level information and with analytical end-point calculations. We find that the kinematical endpoint of the $m_{\tau^+\tau^-}$ distribution can be reconstructed with 16 fb^{-1} of data, using a linear fit and tau1P tau reconstruction. A sample of $Z \to \tau\tau$ is used as a reference for the performance studies.

ATL-PHYS-PUB-2006-021
22 July 2006

1 Introduction

Several models of new physics at the LHC include soft taus ($p_T \lesssim 30$ GeV) as an important experimental signature. Models based on SUper SYmmetry (SUSY) [1] are amongst these, depending on the particular model and parameters chosen. Soft taus can act as an important handle on information of the underlying physics, and the ability to reconstruct these particles can therefore be crucial. The soft nature of the taus, together with the high multiplicity environment in SUSY events, makes the reconstruction of such particles a particularly challenging task.

In this note, we study and work on the soft tau reconstruction performance of two tau reconstruction algorithms specific to the ATLAS detector, tauRec [2] and tau1P3P [3]. We primarily use a data set from the *stau coannihilation* [4] region of *minimal SUperGRAvity* (mSUGRA) [5] parameter space. An overview of this model is given in section 1.1. In addition, we use a $Z \to \tau\tau$ data set as a reference. ATLAS release 9.0.4 [12] was used for reconstructing the two samples.

The principles of the two algorithms are described in section 1.3. In section 2, we study the performance of the two reconstruction algorithms under different conditions. In section 3, we use the algorithms to reconstruct the invariant mass of tau pairs from the decay chain $\chi_2^0 \to \tilde{\tau} + \tau; \tilde{\tau} \to \tau + \chi_1^0$ in the stau coannihilation sample.

1.1 mSUGRA stau coannihilation region

SUSY is a symmetry predicting that every particle has a partner with identical quantum numbers, except for spin, which differs by $\pm 1/2$ between the partners. This is incorporated in the *Minimal Supersymmetric Standard Model* (MSSM)[1], currently one of the most promising extensions of the Standard Model (SM)[6]. MSSM has three desirable features: it provides a natural cancellation of higher order corrections to the Higgs mass, it unifies the electroweak (EW) and strong force at a scale of $\mathcal{O}(10^{16})$ GeV, and it provides a candidate for the dark matter in the Universe.

The partners to the SM particles are referred to as *super partners*, with scalar *sfermions* as partners to the ferminos, and fermionic *gauginos* and *higgsinos* as partners of bosons.

If the super partners were identical to the SM particles in every respect expect for spin, they should already have been observed at several experiments. Since this is not the case, it forces us to conclude that if SUSY is to exist, the symmetry must be broken in such a way that the super partners obtain masses large enough to have escaped detection so far.

MSSM adds 105 new free parameters to the 19 SM parameters [5], making the parameter space very complex. To cope with this, several ways of constraining the parameter set exists, among those mSUGRA. This model reduces the parameter set to five free parameters by assuming that the breaking of SUSY is mediated by gravity, and that SUSY therefore is unbroken at the GUT (Grand Unified Theory) scale of $\mathcal{O}(10^{16}\text{GeV})$. Exploiting this fact, one can express the parameters of the model at the unified scale and use the renormalization group equations (RGE) to calculate the corresponding parameters at the EW scale.

The mSUGRA parameter set consists of m_0 and $m_{1/2}$ (sfermion and gaugino masses), A_0 (Higgs-sparticle trilinear interaction terms), $tan\beta$ (relating the vacuum expectation values of the neutral components of the Higgs doublets $H_{d/u}$), and finally the sign of μ, the higgsino mass parameter.

1.1.1 Cold Dark Matter candidate in mSUGRA

Studies of the rotational velocities of galaxies as well as measurements from the *Wilkinson Microwave Anisotropy Probe* (WMAP) [7] indicate that a large part of our Universe consists of an as yet unknown type of matter, referred to as *Cold Dark Matter* (CDM).

In order not to conflict with observations, different sets of required properties for a dark matter candidate exists. One of these is the *Weakly Interacting Massive Particle* (WIMP), which also is required to be stable, necessary in order to prevent the dark matter from decaying to known particles. In most mSUGRA scenarios, R-parity is imposed in order to make the proton stable. This ensures also that the *Lightest Supersymmetric Particle* (LSP) is stable. If the LSP then also is massive and only weakly interacting, it fulfils the requirements for a CDM candidate. For most of mSUGRA parameter space, this is indeed the case, as the LSP is the lightest neutralino, χ_1^0, a particle that should produce observable effects in terms of a detectable amount of E_T^{miss} in ATLAS.

1.1.2 Relic density and WMAP-allowed regions of mSUGRA parameter space

For χ_1^0 to be a valid CDM candidate, its density in the Universe today needs to be consistent with the WMAP measurements. This density is referred to as the *relic density*,

and can be calculated for any mSUGRA parameter point, based on the estimated production/annihilation rates in the thermal equilibrium of the early Universe.

In this way large parts of the parameter space are excluded by prediction of too high relic density, and some "WMAP-allowed" regions can be identified [8]. The various allowed regions in mSUGRA parameter space rely on different annihilation channels for the correct relic density. The parameter point we use in this study lies in the the stau coannihilation region, where the process $\chi_1^0 + \tilde{\tau}_1 \rightarrow \tau + Z^0/\gamma$ is one of the most important coannihilation channels, hence the name.

Features more particular to the specific parameter point used in this study are covered together with the analysis itself in section 3.

1.2 Tau decays

Tau decay modes are classified in two main groups: leptonic and hadronic. The leptonic decay channels of taus (35.2% branching fraction) [5], $\tau \rightarrow \nu_\tau + l + \nu_l$ are considered hard to use for the purpose of tau identification, since it is hard to distinguish between primary leptons and leptons from tau decays. The tau lifetime of 2.9×10^{-13} s results in a very small impact parameter for the track of the leptonic decay product, while the neutrino escapes the detector, leaving no visible vertex for identification.

Hadronic decay modes ($\tau \rightarrow \nu_\tau + hadrons$) have a total branching fraction of 64.8%. The basic task of the identification procedure is to distinguish these hadronic decay products of a tau, the tau "jet", from those of QCD jets. Lower multiplicity in the tau jet compared to a QCD jet is one of the key discriminating properties. The tau primarily decays into one charged particle (one prong decay, 49.5%,) or three charged particles (three prong, 15.2%) accompanied by a neutrino. In $\sim 60\%$ of the hadronic decays there are one or more π^0 accompanying the charged hadrons. This results in an important electromagnetic energy component in the tau jet.

1.2.1 Tau decay generation

As neutrinos escape detection, visible hadronic energy from tau decay must serve as an estimate of the tau energy. For a given process, it is therefore important to reliably relate the visible hadronic energy distribution to the tau energy distribution, using information from a Monte-Carlo generator. We study the distribution of the ratio of visible transverse energy from the hadronic decay products of the tau (E_T^{hadr}) to the total tau energy (E_T^{total}) in the Herwig[9] 6.505 and Pythia[10] 6.203 generators, see figure 1. Herwig was used for generating the SUSY sample studied in this note, while Pythia was used for the $Z \rightarrow \tau\tau$ sample. We observe that the distributions from the Herwig generator is unphysical, since it consists of a superposition of flat distributions, characteristic for two-body decays. The sharp edges are due to the fact that the meson width is absent from the Herwig generator, leaving intermediate mesons in tau decays with no width. We have verified that this feature has only minute effects for reconstructed variables like invariant mass of two taus, but should nevertheless be kept in mind.

1.3 Tau reconstruction in the ATLAS Detector.

In this study, we have used two publicly available tau reconstruction algorithms for the ATLAS detector, *tauRec* and *tau1P3P*. Both algorithms aim to reconstruct the *visible*

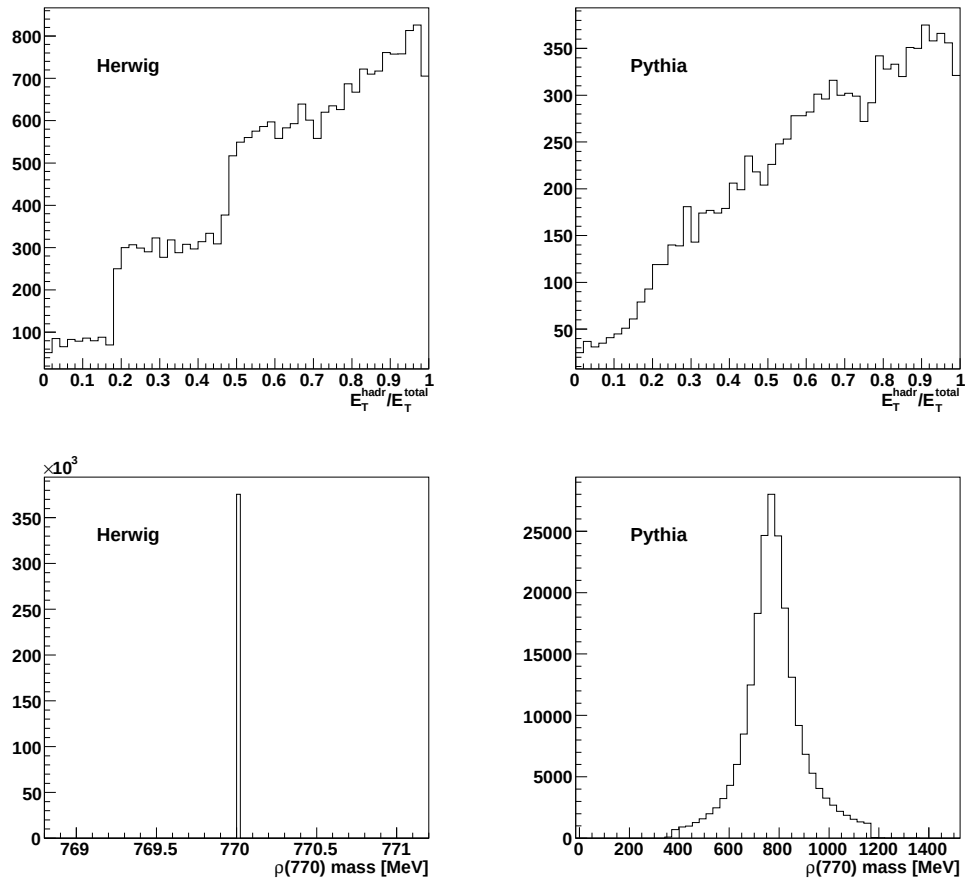

Figure 1: Upper row: The fraction of E_T of the hadronic tau decay products to the E_T of the initial tau (E_T^{hadr}/E_T^{total}) in Herwig and Pythia. The step-like distribution in Herwig, consisting of superposition of flat distributions characteristic for two body decays, is due to the fact that mesons have no width in Herwig, as can be seen in the lower row, where the mass distribution of $\rho(770)$ is shown.

transverse energy of the hadronic decay products of the tau. In the following, when we write about the reconstructed E_T of the tau, we therefore mean the reconstructed transverse energy of the hadronic decay products.

1.3.1 tauRec

The default tau reconstruction algorithm in ATLAS is tauRec. It is "seeded" (initiated) either by a *CombinedCluster* from the *CaloClusterBuilderSW* or by a reconstructed track, creating a *tau candidate*. The first option is the default. The *CaloClusterBuilderSW* algorithm sometimes creates overlapping clusters, resulting in overlapping tau candidates. We resolve these overlaps by choosing the tau with the highest E_T^{rec} in a cone $\Delta R < 0.4$, where $\Delta R = \sqrt{\Delta\eta^2 + \Delta\phi^2}$. Once seeded, the algorithm collects cell energies and tracks in different cone sizes around the initial seed, calculating calorimetric variables using the H1 calibration [11] procedure for calibrating the collected energy. Finally it calculates a likelihood for each tau candidate. The likelihood calculation is based on probability distributions functions (PDFs) of six variables:

- *Electromagnetic radius* : $(\Sigma\Delta R \cdot E_T^{cell})/(\Sigma E_T^{cell})$ measure of the radius of energy deposition in EM calorimeter in cone $\Delta R < 0.4$ around seed.
- *Isolation fraction* : ΣE_T^{cell} in cone $0.1 < \Delta R < 0.2$ divided by ΣE_T^{cell} in $\Delta R < 0.4$.
- *(Strip Width)*^{2} : Variance of η in strip layer (layer 1 in EM calorimeter), weighted by deposited energy in cone $\Delta R < 0.4$. See section 2.4.
- *Number of strips* : Number of strip layer cells in $\Delta R < 0.4$ associated with the candidate.
- $E_T^{rec}/p_T^{leadingtrack}$: Reconstructed E_T over p_T of the highest momentum track.
- $d0/\sigma_{d0}^2 \cdot sign(sin(\phi^{rec} - \phi^{leadingtrack}))$: impact parameter $d0$ significance of the leading track.

1.3.2 tau1P3P

tau1P3P is the other tau reconstruction package used in this analysis. The stand alone version of the package is used, since it is not yet fully integrated with *Athena* [12], the ATLAS software framework. The package consists of two algorithms, *tau1P* and *tau3P*, for reconstructing 1-prong and 3-prong taus respectively. Both the tau1P and the tau3P algorithm use *qualified tracks* (tracks passing the quality cuts $d0 < 1$ mm, #TRT hits > 9, #SCT+#Pixel hits> 8 , $|\eta| < 1.5$ and $\chi^2 < 1.7$) as seeds, and an energy flow algorithm for collecting the jet energy. Equation 1 shows the different components used for calculating the energy [3, 13].

$$E_T^{flow} = E_T^{emcl} + E_T^{neuEM} + \Sigma p_T^{track} + \Sigma res E_T^{chrgEMtrk} + res E_T^{neuEM} \quad (1)$$

Important to notice is that the momenta of the seed-tracks (Σp_T^{track}) are used in the energy calculation, exploiting the fact that the momentum resolution of tracks is better than that of the calorimeter for low energies. The prevailing type of neutral hadron, π^0, will

decay to photons before reaching the calorimeter. This energy (E_T^{emcl} and E_T^{neuEM}) is collected using energy deposits in EM calorimeter *not* matching a track, but still within a cone $R < 0.2$ with respect to the track at vertex. The two remaining terms are parametrized corrections for residual effects.

Instead of a likelihood, PDE-RS (*Probability Density Estimation based on Range Searching*) [15] is used as the method for discrimination of real taus from background. This discrimination technique is similar to the likelihood method, in the sense that it compares each reconstructed tau to a preclassified sample. The variables used to construct probability densities and thus to select the signal are listed below, and several of the variables are the same as in tauRec.

- *Electromagnetic radius*: same as tauRec, but in cone $\Delta R < 0.2$
- *Isolation fraction*: Same as for isolation fraction in tauRec, but in cone $\Delta R < 0.2$.
- *(Strip Width)*^{2}: same as tauRec, but in cone $\Delta R < 0.2$
- *Number of strips*: same as tauRec, but in cone $\Delta R < 0.2$
- $E_T^{rechad}/p_T^{leadingtrack}$: E_T of hadronic cells over p_T of leading track.
- $(E_T^{otherEM} + E_T^{otherHad})/E_T^{calo}$: E_T in cone $0.2 < \Delta R < 0.4$ for EM and Had calorimeter, divided by total ΣE_T^{cell} in $\Delta R < 0.4$.

At present, tau1P3P reconstructs taus in the ATLAS barrel region only, $|\eta| < 1.5$, although there is no deep reasons for this limitations other than a clean environment, both in terms of physics and detector. It also uses an MC veto on tracks from muons and electrons (thus not taking the lepton identification efficiency into account). The reason for this is that there was not any mature package to veto lepton tracks at the time the algorithm was implemented.

2 Performance studies

In this section, we present the performance of the two algorithms on a stau coannihilation region sample (see section 1.1) and on a $Z \to \tau\tau$ sample. We first study performance of both methods with default settings, and then with possible optimisations. Our optimization efforts have mainly been focused on tau1P3P. We also present energy and angular resolutions, and study to which degree the two algorithms reconstruct the same taus.

2.1 Samples used in this study

Figure 2 shows the generated true E_T distribution for true taus and their hadronic decay products.

Both samples come from Data Challenge 2 (DC2) production:

- SUSY coannihilation DC2 sample: `dc2.003028.A9_susy`.
- $Z \to \tau\tau$ DC2 sample: `dc2.003004.A3_z_tau_tau`.

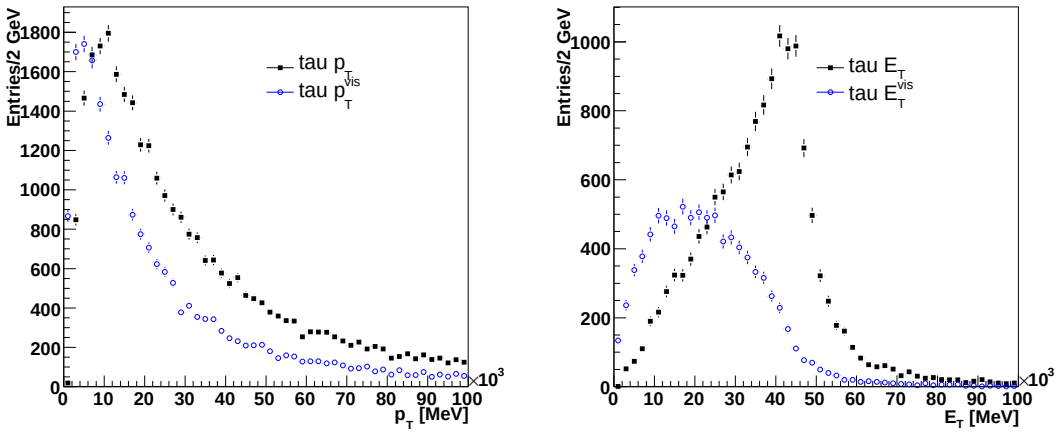

Figure 2: Generated tau E_T distributions for SUSY coannihilation sample (left) and $Z \to \tau\tau$ (right). Shown are both the E_T for the tau and for the visible hadronic decay products. Since only 64.8% of the taus decay hadronically, the histograms have different area.

	events	$\#\tau$	$\#\tau \to$ had	τ $\lvert\eta\rvert < 1.5$	$\tau \to$ had$\lvert\eta\rvert < 1.5$
SUSY coann	111000	63423	41167	49451	32048
$Z \to \tau\tau$	23900	48986	30867	19488	12296

Table 1: Number of taus in the two data samples used in this analysis.

Both data sets were reconstructed with ATLAS software release 9.0.4. The number of events, taus, hadronic taus and taus within $|\eta| < 1.5$ in these samples are summarised in table 1. In addition, a sample of 30250 SUSY events and 10560 $Z \to \tau\tau$ events was used as PDE-RS training sample. These samples contain respectively 8779 and 5336 hadronically decaying taus with $|\eta| < 1.5$.

2.2 Performance with default settings

We start by evaluating the performance of both algorithms with default settings. Since tau1P3P is limited to $|\eta| < 1.5$, we also limit tauRec to this range. Since tau1P3P has a MC truth veto on electron and muon tracks, we impose the same requirement on tauRec, assuming that the tendency to take an electron or muon for a tau is similar for the two algorithms.

The reconstruction efficiency ϵ is defined in equation 2 and the jet mistag rate ρ in equation 3.

$$\epsilon = \frac{\#\text{rec } \tau \text{ matched to true hadr } \tau \text{ in cone } \Delta R < 0.2}{\#\text{true hadronic decaying } \tau\text{s in} |\eta| < 1.5} \tag{2}$$

$$\rho = \frac{\#\text{rec } \tau \text{ not matched to true hadr } \tau \text{ in cone } \Delta R < 0.2}{\#\text{jets in } |\eta| < 1.5} \tag{3}$$

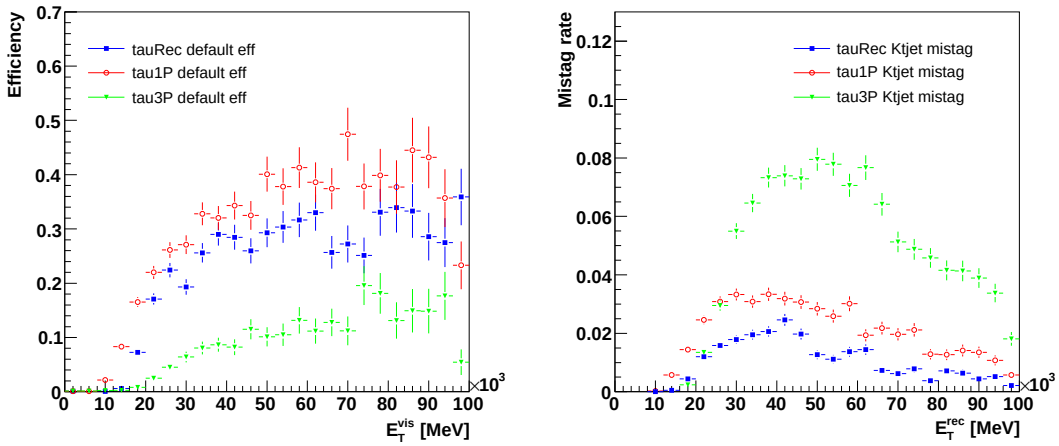

Figure 3: Efficiency and mistag rate for tauRec, tau1P and tau3P with default settings, evaluated from the reconstructed SUSY sample. The mistag rate is evaluated against jets reconstructed by the default KtJet[14] algorithm in ATLAS release 9.0.4. Overlap between reconstructed jets and reconstructed taus have not been removed when calculating mistag rate.

Figure 3 shows to the left the efficiency vs true visible E_T of the hadronic decay products for default tauRec, tau1P and tau3P. For tau1P3P there is no default cut for the PDE-RS discriminator variable, so we use 0.5 as an ad-hoc default setting. The mistag rate is shown in the right plot. The performances of tauRec and tau1P are at a comparable level, while tau3P shows lower efficiency and higher mistag rate. Since only 21% of the hadronic tau decays are three-prong decays, the lower efficiency is expected, but the far higher mistag rate results in an overall poor performance for tau3P. The high mistag rate is most likely due to three-prong jets being more similar to ordinary QCD jets in terms of multiplicity.

The higher efficiency at low energies of tau1P compared to tauRec is partly explained by tau1P having a cut $p_T > 10$ GeV for the track used as seed, while tauRec has cut $E_T > 15$ GeV on its calo cluster seed. In general, the efficiency for tau1P is higher, but at the same time it shows a higher jet mistag rate.

Figure 4 shows the fraction of true one-, three- and five prong decays reconstructed by the three algorithms. We see that tauRec and tau1P performs similar also in this respect, tauRec reconstructing 6.5% more three prong taus than tau1P.

Because of the small gain in efficiency compared to the large mistag rate introduced by tau3P, we will from now on use only the tau1P part of tau1P3P. Since we observe that tau1P and tauRec reconstruct a similar fraction of one-prong/three-prong decays, a comparison of the algorithms is still justified.

2.3 Track isolation in tau1P

For the tau1P algorithm to be seeded by a track, the track is required to be isolated. This means that there should be no other qualified tracks in a cone $\Delta R < 0.2$ around the track (see section 1.3.2 for definition of qualified track).

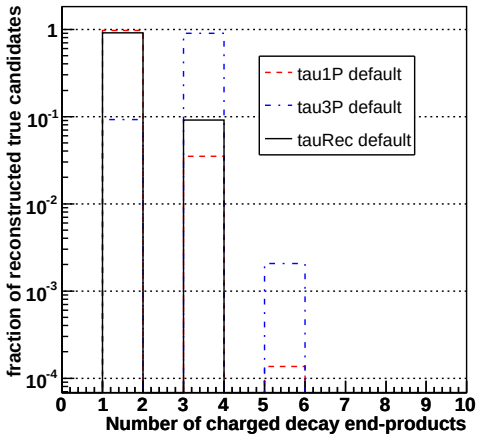

Figure 4: Fraction of true one-, three- and five-prong decays reconstructed by each algorithm.

The number of *non-qualified* tracks around a candidate could also be used as a selection variable, and figure 5 shows the number of unqualified tracks around true and false tau1P candidates in the SUSY and $Z \to \tau\tau$ sample. We observe that there is a clear correlation between the number of non-qualified tracks around true and false candidates in the SUSY sample. The correlation is present also in the $Z \to \tau\tau$ case, but it is not so pronounced. This difference is due to the large number of tracks and jets in the SUSY events compared to the $Z \to \tau\tau$ sample, shown in figure 6.

Loosening the qualified track criteria for surrounding tracks could possibly reject some of the background. Figure 7 shows the track parameters for non-qualified tracks surrounding true taus (upper row) and false taus (lower row). We observe that the track parameters are distributed very similarly for true and false candidates, and fine-tuning the qualification criteria will not gain further rejection.

We therefore require the number of both qualified and unqualified tracks around a leading track to be zero, which in the SUSY case rejects a significant part of the background. This can be seen in figure 8, where all other cuts are kept at their default values. We see that the mistag rate is reduced compared to the default performance obtained in figure 3.

The obtained efficiencies are summarised in section 2.5, table 3, together with results for other variations in cut values.

2.4 Calorimeter noise impact on rejection

Figure 9 shows the tauRec likelihood and tau1P PDE distributions for a default setup of the algorithms. The tauRec likelihood distribution clearly shows a "repeating" structure, with a second group of true and false candidates at likelihood< -10. The corresponding PDE distribution looks as expected from a discriminator distribution.

It turns out the likelihood "groups" are strongly correlated with the *(strip width)*^{2} quantity (equation 4), as can be seen from the right hand plot in figure 10. The strip

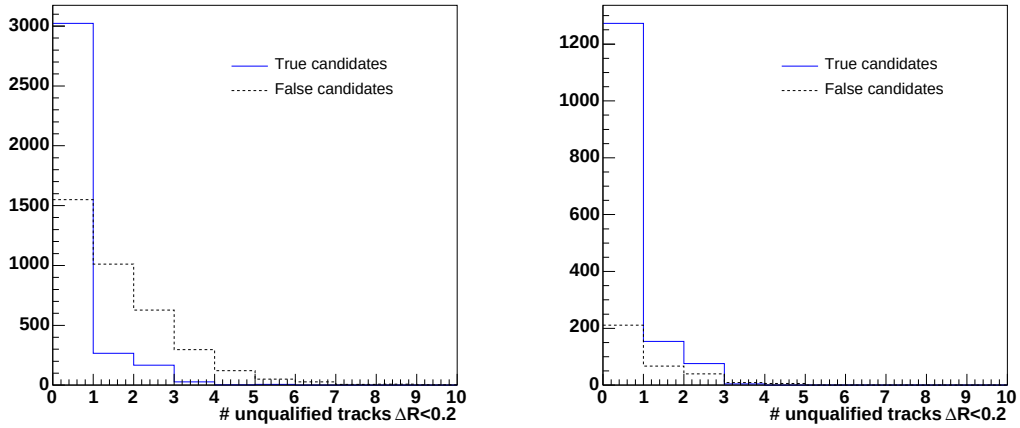

Figure 5: Number of unqualified tracks surrounding true and false tau1P candidates in SUSY sample (left) and $Z \to \tau\tau$ sample (right).

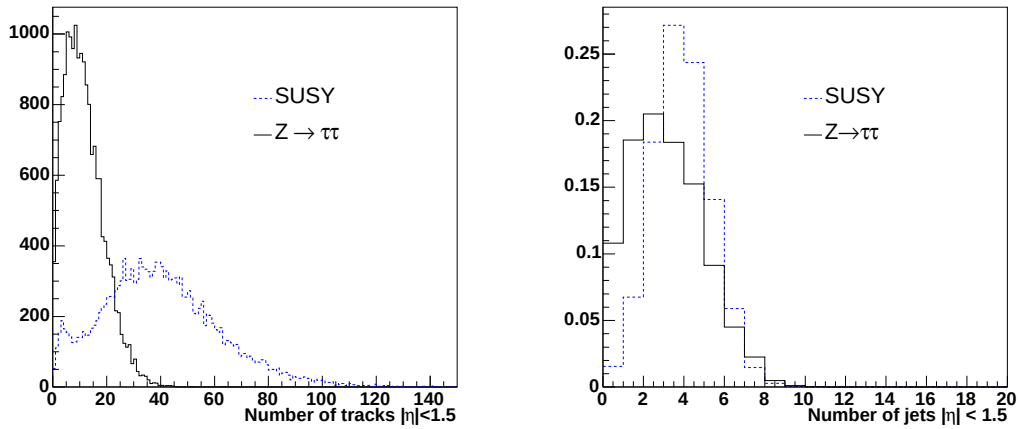

Figure 6: Number of tracks (left) and jets (right) with $|\eta| < 1.5$ in the two samples.

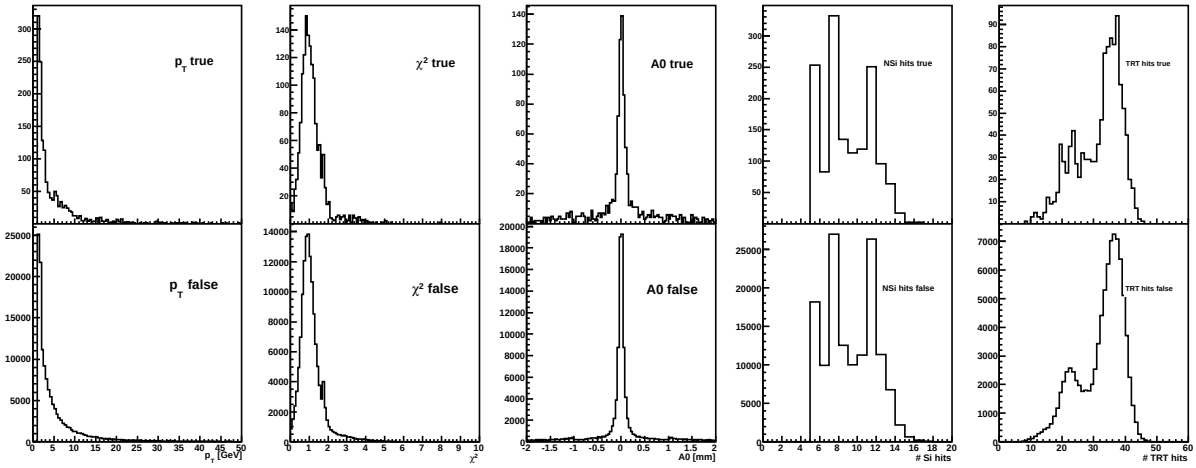

Figure 7: Track parameters for unqualified tracks surrounding a tau1P candidate. The upper row shows the unqualified tracks surrounding true candidates, while the lower row shows the unqualified tracks surrounding false candidates.

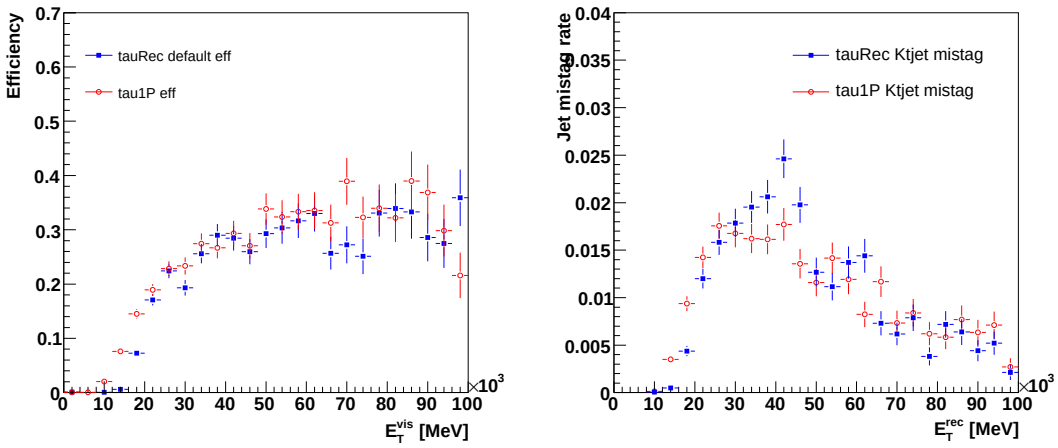

Figure 8: Efficiency and mistag rate for tauRec and tau1P when requiring both number of qualified and unqualified tracks around a leading track to be zero for tau1P.

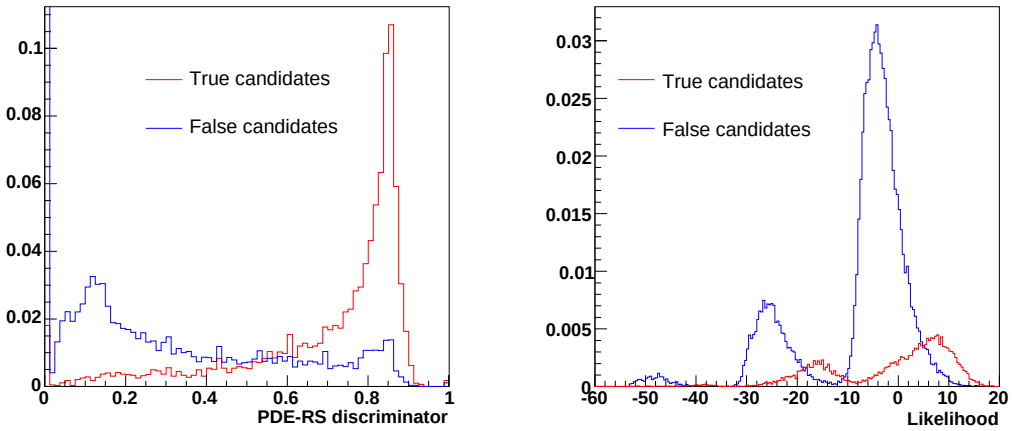

Figure 9: Discriminator distribution for default setup of tau1P PDE-RS (left) and tauRec likelihood(right) on SUSY dataset.

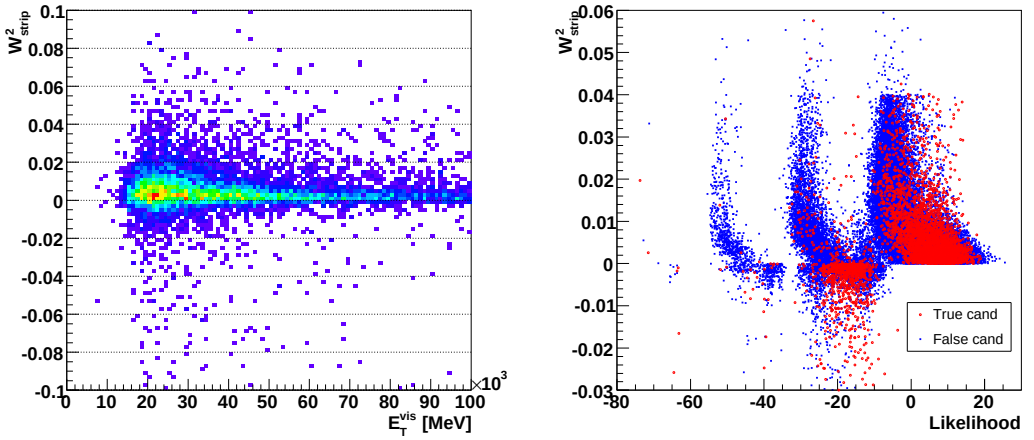

Figure 10: Left: W^2_{strip} vs E^{vis}_T for tauRec candidates in SUSY sample. Right: W^2_{strip} vs likelihood in SUSY sample.

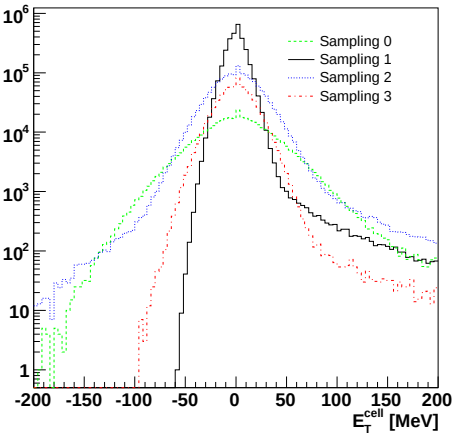

Figure 11: E_T for all cells in $|\eta| < 1.5$ in the four layers of the EM calorimeter.

width is the energy weighted variance of the eta distribution of cells in EM sampling layer 1, also called the *strip layer*:

$$W^2_{strip} = \frac{\sum \eta^2 \cdot E_T^{cell}}{\sum E_T^{cell}} - \frac{(\sum \eta \cdot E_T^{cell})^2}{(\sum E_T^{cell})^2} \tag{4}$$

As can be seen from the formula, negative values of E_T^{cell} can lead to a negative W^2_{strip}. Negative E_T^{cell} values are due to noise in the calorimeter, and can be seen as the negative component in figure 11, showing E_T for all cells in the EM calorimeter.

A plot of W^2_{strip} vs E_T^{vis} is shown to the left in figure 10. The distribution of W^2_{strip} widens for lower E_T, increasing the fraction of candidates with negative W^2_{strip}. As negative W^2_{strip} is not a valid range in the PDF used for calculating the likelihood, the candidates get a very low likelihood, effectively rejecting them. The same effect can be seen for true taus outside the limits of the other PDFs, but negative W^2_{strip} is by far the dominating rejection factor. In the following, we will reject all candidates with values outside the PDF ranges.

The same effect is also clearly visible in the $Z \to \tau\tau$ likelihood, see figure 12. In fact, here the effect of negative W^2_{strip} is even larger, since almost all taus have a hadronic $E_T <$ 50 GeV, see figure 2. As shown in figure 10, this is the region where the negative W^2_{strip} starts to get pronounced.

For tau1P the default E_T^{cell} cut is 100 MeV, so no negative contribution is included in the W^2_{strip} calculation. However, in some cases none of the cells passes the cut, resulting in a W^2_{strip} of zero. These candidates are rejected *before* entering the PDE calculation, and are thus not visible in the discriminator distributions.

According to figure 11, the cut on E_T^{cell} could be lowered to 50 MeV to allow for a smaller fraction of zero W^2_{strip} candidates, at the cost of introducing somewhat more noise hits in the energy collection.

Table 2 shows the percentage of true tau candidates rejected solely due to negative/zero strip width, and the impact of this is higher for tauRec than for tau1P. By lowering the

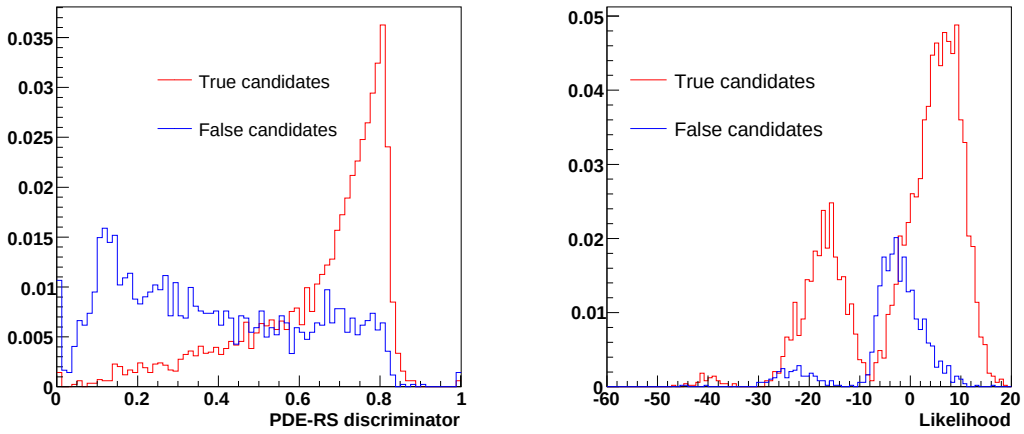

Figure 12: PDE-RS discriminator distribution for default run of tau1P (left) and likelihood distribution for default run of tauRec (right) for $Z \to \tau\tau$ dataset.

	SUSY	$Z \to \tau\tau$
true tauRec 15 GeV candidates	$25.4 \pm 0.5\%$	$27.1 \pm 0.7\%$
true tauRec 5 GeV candidates	$29.1 \pm 0.6\%$	-
true tau1P 10 GeV candidates, E_T^{cell} cut 100 MeV	$20.7 \pm 0.5\%$	$26.0 \pm 0.8\%$
true tau1P 10 GeV candidates, E_T^{cell} cut 50 MeV	$13.0 \pm 0.5\%$	-
true tau1P 5 GeV candidates, E_T^{cell} cut 100 MeV	$23.4 \pm 0.5\%$	$25.1 \pm 0.6\%$
true tau1P 5 GeV candidates, E_T^{cell} cut 50 MeV	$14.2 \pm 0.4\%$	-

Table 2: Percentage of true candidates rejected solely due to negative/zero W^2_{strip}. We see that the cut on E_T^{cell} has a clear impact on the rejection for tau1P.

E_T^{cell} cut to 50 MeV for tau1P, we recover 5 - 10 % of the previously rejected candidates, as this allows for the low E_T tau candidates to aquire a non-zero W^2_{strip}. The impact on background rejection due to this change is very small, as will be shown in section 2.5.

2.5 Reconstruction efficiency vs background rejection

In this section, we study the relation between reconstruction efficiency and background rejection as a function of likelihood and PDE cuts. An often useful quantity to display is the rejection against jets, as given in figure 3. The problem in this case is that for taus with $E_T < 15$ GeV, we do not have any jets, as jets with $E_T < 15$ GeV are not output by the jet reconstruction. Therefore, in order to be able to compare performance on an equal footing for different E_T or p_T seed cuts, we use the fraction of false candidates in the reconstructed sample (eq. 5) as a measure of purity. We plot this quantity against the reconstruction efficiency, already defined in equation 2.

$$\text{False candidates fraction} = \frac{\#\text{ Number of false candidates}}{\#\text{ Total number of candidates}} \tag{5}$$

We change the cut on the tauRec likelihood in steps of two from -10 to 14, and in steps of 0.05 from 0 to 0.9 for tau1P PDE-RS. The reason we do not scan the full range is to avoid the edges of the discriminator distributions (see figure 9), where the performance becomes highly unstable.

From these scans, we plot efficiency vs fraction of false candidates. The result for the SUSY sample is shown in figure 13 for different conditions of the algorithms. It is important to keep in mind that since this is a sample containing the whole range of SUSY processes given by our parameter point, not all events included in the analysis contain the desired tau pair decay chain.

From the plots it is clear that tau1P and tauRec show different efficiency vs fraction of false candidates dependencies: tauRec gives a higher purity for $\epsilon < 0.1$, while tau1P performs better for higher efficiencies.

For tau1P, the best results are obtained requiring a completely isolated track, $p_T^{seed} > 5$ GeV and $E_T^{cell} > 50$ MeV cutoff, as seen in figure 13. We will refer to these settings as *optimized*, and use them for the rest of the study, unless otherwise noted. For tauRec the optimal settings vary with region of the scan, so it is not clear which settings give the overall best performance. We therefore choose to use the default settings, $E_T^{cluster} > 15$ GeV.

The performance for the different settings with default discriminator cutoff are given in table 3, while the efficiency vs true E_T^{vis} for the optimized tau1P settings is shown in figure 14 together with the default efficiency for tau1P.

We perform some of the same scans for the $Z \rightarrow \tau\tau$ sample, shown in figure 15, and notice that both a higher purity and a higher efficiency is obtained compared to the SUSY case. The increased performance is most likely due to a combination of the cleaner topology of the sample, the fact that each event contains a tau pair and finally that the taus have on average higher transverse energy compared to the taus in the SUSY sample.

2.5.1 Impact of PDE-RS classification sample on performance

In the performance scans for tau1P, we used the same type of sample both for analysis and for PDE-RS classification. To investigate what is the impact of the classification sample on the performance, we use a $Z \rightarrow \tau\tau$ sample as classification sample when analysing the SUSY sample. The performance curve can be seen in figure 13, and we see that this is reducing the performance of tau1P, indicating that the variables used for PDE-RS are not uncorrelated with energy, as would also be expected.

2.6 E_T resolutions

We define the resolution of the tau E_T reconstruction to be the sigma of a gaussian fit to the distribution E_T^{rec}/E_T^{vis}, where E_T^{vis} is the usual true transverse energy of the hadronic decay products. The resolution is dominated by two components: the intrinsic resolution of the detector, and to which degree the reconstruction manages to correctly collect the hadronic energy of the tau. As the two algorithms in this study use quite different techniques, see section 1.3, some differences are expected.

The E_T^{rec}/E_T^{vis} distributions for tauRec and tau1P with fitted gaussians are shown in figure 16. For tauRec, the energies have been multiplied by 1.08 to account for the miscalibration introduced due to the use of Geant3 weights.

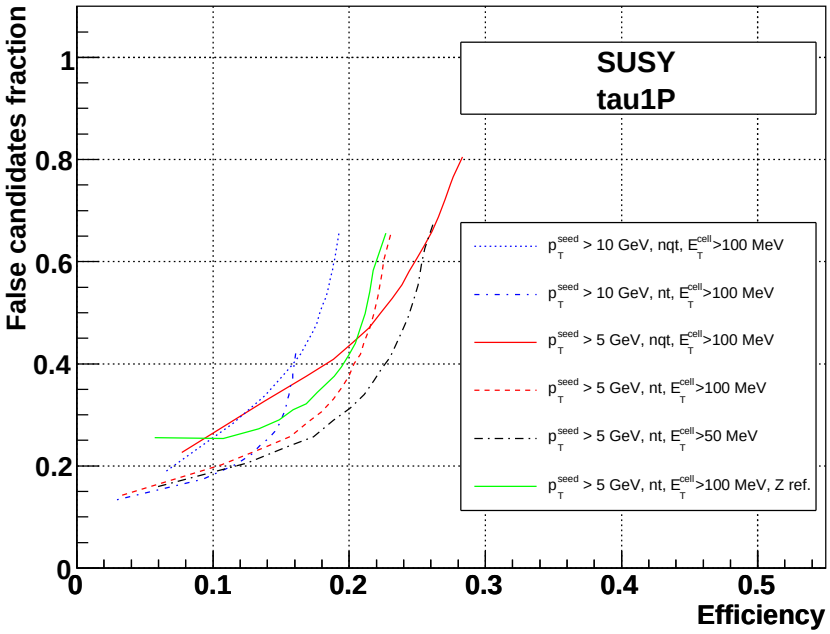

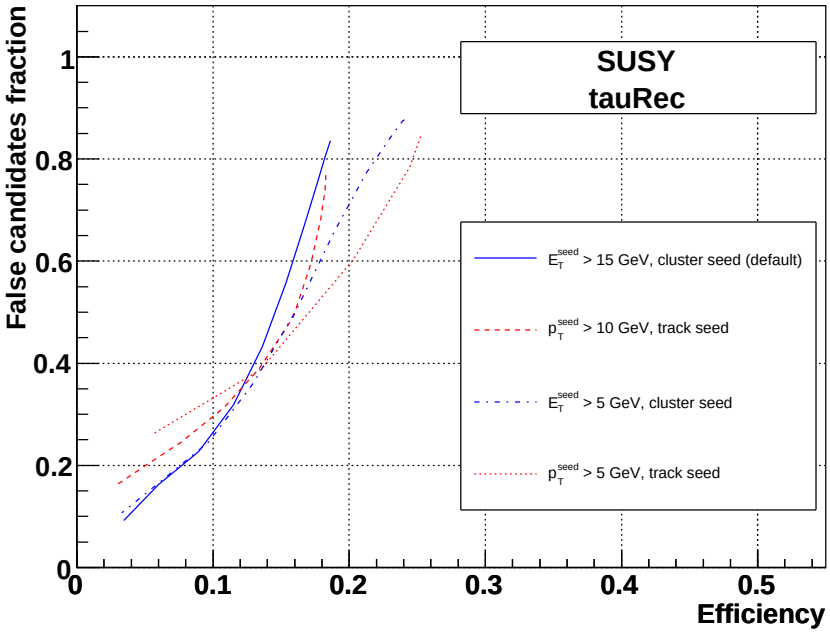

Figure 13: Fraction of false candidates vs efficiency for the two algorithms run on the SUSY sample. Explanation to the notation used in the legend: **tau1P**: p_T^{seed} - track seed cutoff; *nqt* - no qualified track around candidate; *nt* - no track around candidate; E_T^{cell} - EM cell cutoff; *Zref* - PDE-RS trained on $Z \rightarrow \tau\tau$ sample;**tauRec**: E_T and p_T: calo/track seed cutoff.

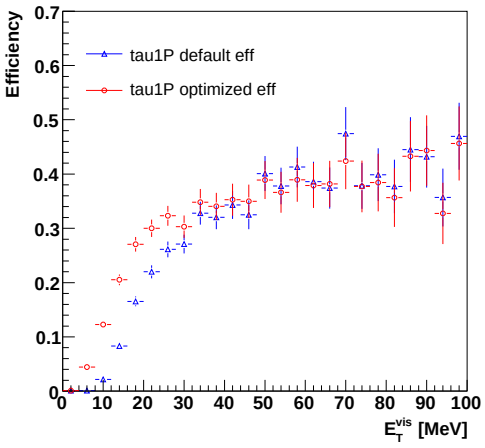

Figure 14: Efficiency with optimized tau1P settings and with default tau1P settings for the SUSY sample. The purity of the optimized settings are better than the default, see table 3.

	SUSY		$Z \to \tau\tau$	
	efficiency	purity	efficiency	purity
tauRec $E_T^{seed} > 15$ GeV, cluster	11.5±0.2%	67.9±0.8%	18.7±0.4%	95.6±0.4%
tauRec $E_T^{seed} > 5$ GeV cluster	13.0±0.2%	61.6±0.8%	-	-
tau1P $p_T^{seed} > 10$ GeV, nqt, $E_T^{cell} > 100$ MeV	17.0±0.2%	52.8±0.7%	21.0±0.4%	92.5±0.5%
tau1P $p_T^{seed} > 10$ GeV, nt, $E_T^{cell} > 100$ MeV	14.5±0.2%	71.1±0.7%	17.5±0.3%	95.3±0.5%
tau1P $p_T^{seed} > 5$ GeV, nqt, $E_T^{cell} > 100$ MeV	22.8±0.3%	46.9±0.6%	29.3±0.5%	88.0±0.5%
tau1P $p_T^{seed} > 5$ GeV, nt, $E_T^{cell} > 100$ MeV	19.2±0.2%	64.2±0.6%	24.1±0.4%	91.1±0.5%
tau1P $p_T^{seed} > 5$ GeV, nt, $E_T^{cell} > 50$ MeV	21.6±0.3%	63.2±0.6%	-	-

Table 3: Efficiency and purity for "default" discriminator cutoff (likelihood = 4 and PDE-RS = 0.5). Purity is 1 - "False candidates fraction" in percent. The optimized settings for tau1P is given in the lower row. We see that the purity increases when requiring the leading track of the candidate to be completely isolated for tau1P. The efficiency is increased by lowering the cut on E_T^{cell} and p_T^{track}.

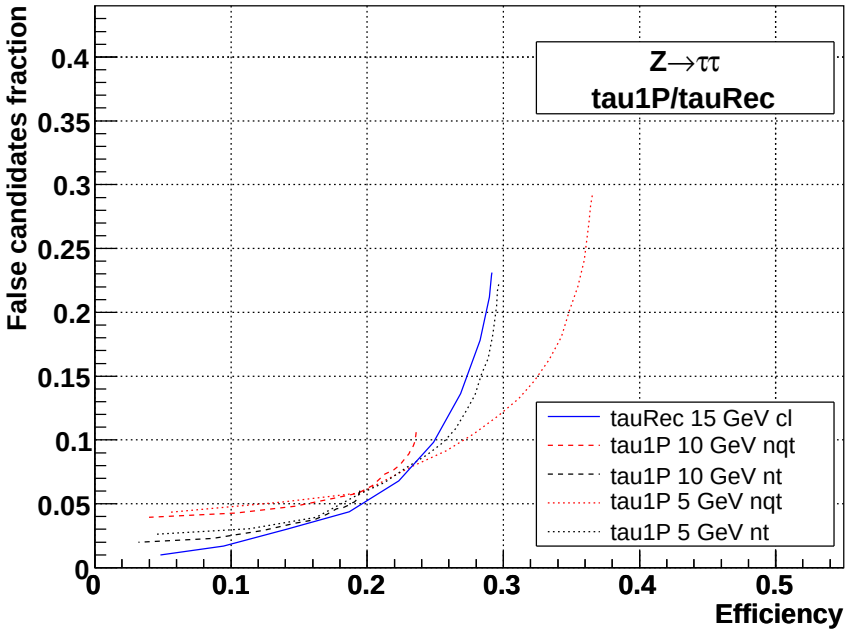

Figure 15: Fraction of false candidates vs efficiency for the two algorithms run on the $Z \to \tau\tau$ sample.

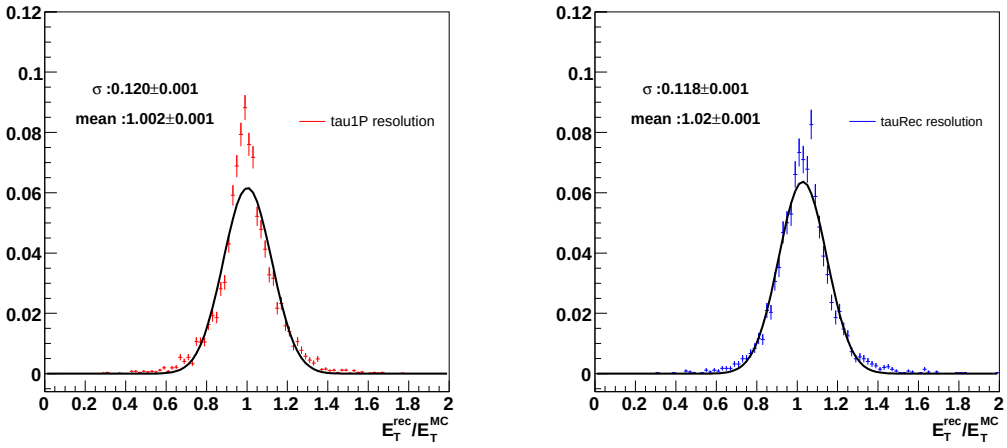

Figure 16: E_T resolution for all candidates for tau1P (left) and tauRec (right) in SUSY sample.

We find that the obtained fit parameters are similar for the two algorithms. Since the resolution is a function of the energy, the distributions shown in figure 16 are superpositions of gaussians with different widths, thus a single gaussian fit to the distribution only indicates the overall resolution scale.

To the left in figure 17, the sigma of the fit to various E_T ranges is given, showing the E_T resolution dependence on the true E_T of the decay products. We see that tauRec resolution improves towards higher energies, while tau1P is more stable, which is most likely due to tau1P using track momenta in the energy calculation, see section 1.3.2.

The E_T dependence of the mean is shown on the right hand side of figure 17. Both algorithms overestimate the reconstructed E_T at low E_T, but at higher energies tau1P starts to underestimate.

2.7 Directional reconstruction

The distance between the reconstructed tau jet and that of the generated tau is calculated using the usual distance measure $\Delta R = \sqrt{\Delta\phi^2 + \Delta\eta^2}$. In figure 18 this quantity is shown for the two algorithms. We see that tau1P reconstructs taus closer to the original tau than tauRec. This is because it is using the position of the leading track at vertex, while tauRec is using the position of the calorimeter cluster, which has a worse spatial resolution, as well as suffering from displacement due to the magnetic field.

2.8 Charge reconstruction

When reconstructing tau pairs, the charge of the tau can be used as a selection criteria, and it is therefore important to have a good charge reconstruction. Figure 19 shows the fraction of taus with correctly reconstructed charge for tauRec and tau1P. For $E_T > 20$ GeV, we see that more than 98% of the taus are reconstructed correctly with respect to charge. From single tracks, we would expect the misidentification of charge to increase with energy [16]. This is however balanced by the fact that more three-prong decays are

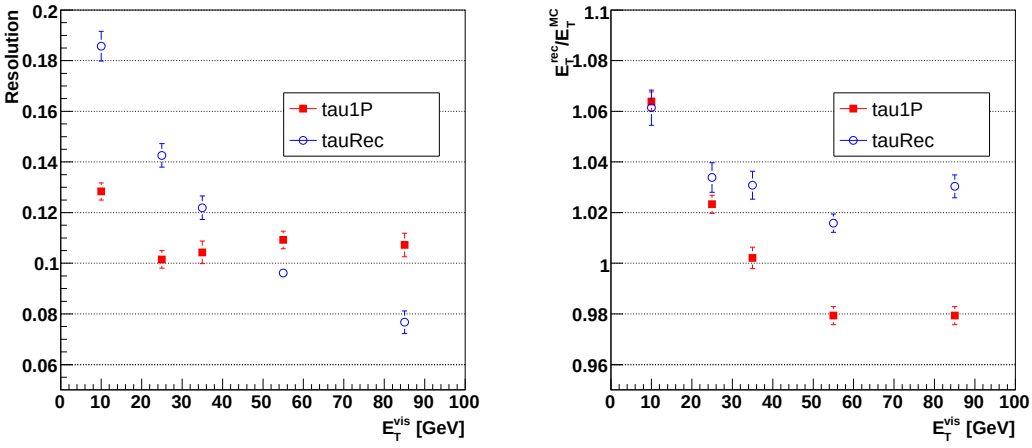

Figure 17: Sigma (left) and mean (right) of gaussian fits to E_T resolution distributions as a function of true visible E_T.

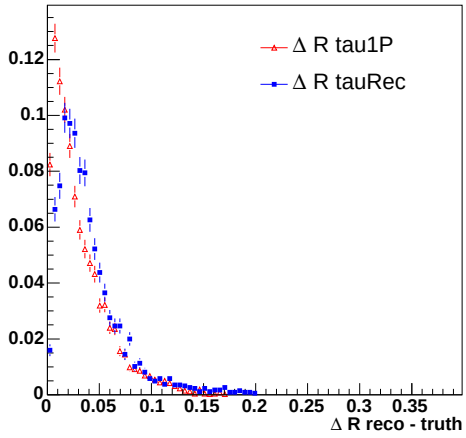

Figure 18: Distance ΔR between reconstructed and true tau for the two algorithms.

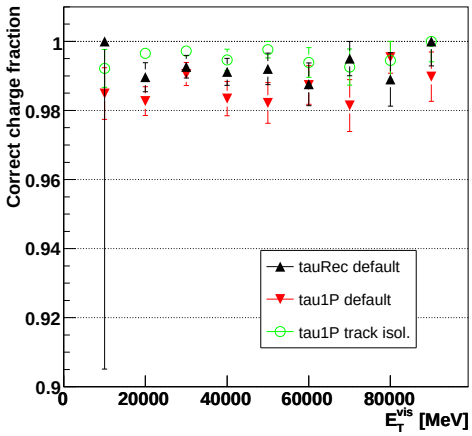

Figure 19: Charge reconstruction for tauRec and tau1P.

	# tauRec candidates	tau1P candidates	matches
true	3698	5456	2198
false	1749	4877	579

Table 4: Matching of true and false candidates from tau1P and tauRec. For both algorithms, the default settings are used, and there are therefore different number of true and false candidates for the two algorithms.

reconstructed at low energies, and that these are more likely to get wrongly reconstructed charge. tauRec has a higher correct charge fraction than the default tau1P, while tau1P with completely isolated track has the highest correct charge fraction, since this more effectively excludes the three-prong contribrution.

2.9 Matching the candidates from the two algorithms

Even if tauRec and tau1P reconstruct a similar number of taus, these are not necessarily the same taus. Matching the reconstructed taus of the two algorithms provides information about how well the two algorithms agree on the true taus. The results are shown in figure 20 and table 4, with a match being defined as one tau candidate from each algorithm in a cone $\Delta R < 0.2$ in the same event. The default tau1P setup was used for this, to have a similar E_T spectrum.

A quite large portion of the true reconstructed taus are only identified by one of the algorithms, suggesting that the two algorithms favour different tau decay characteristics.

The left figure shows that tau1P in general reconstructs a lower E_T than tauRec, in agreement with figure 17. The plot to the right shows the fraction of true tauRec candidate matching a true tau1P candidate as a function of E_T of the tauRec candidate. As E_T increases, so do the probability of having the same tau reconstructed by both algorithms.

As the two algorithms use different approaches for reconstruction, it is indeed expected that different sets of taus are reconstructed by the two algorithms. This effect should be

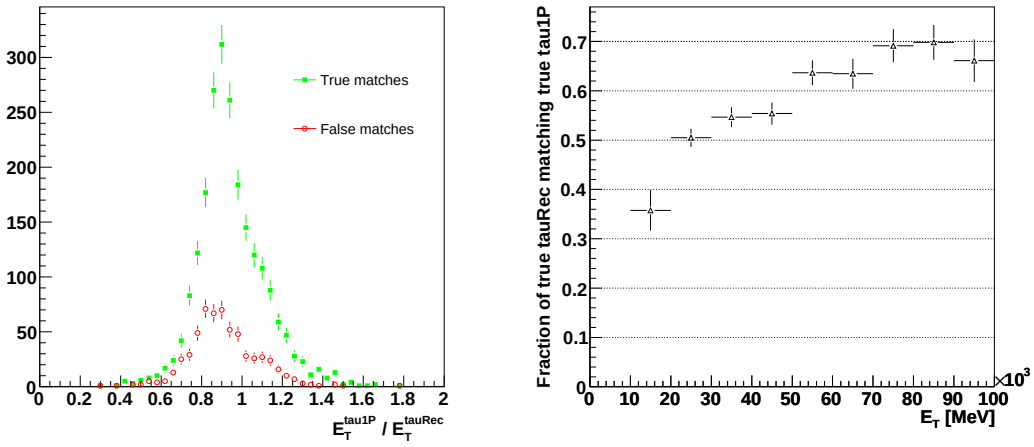

Figure 20: Matching of reconstructed candidates from tau1P and tauRec. To the left is shown the ratio of the reconstructed E_T of matching candidates. To the right is shown the fraction of true tauRec candidates matching a true tau1P candidate, as a function of E_T of the tauRec candidate.

particularly apparent when most of the taus lies in the limit of energy acceptance, as is the case in this study. The comparison shown here should therefore be interpreted as a study of the overlap between the two reconstructed tau sets. For purely algorithmic comparison, we would have to limit the test to contain only taus that *in principle* could be reconstructed by both algorithms.

2.10 Discrimination with a neural network

We check whether using a neural network instead of the PDE-RS method can give an improved separation between true and false candidates for tau1P. As input to the neural network, we use the same variables as for PDE-RS (sec. 1.3.2). We use a package intended for evaluating neural network performance [17], using a four layer 6:5:4:2 (number of nodes in layer) neural network. The package is written in such a way that the training and analysis sample are overlapping, so effects of overtraining have to be kept in mind. However, if we train the network on a sufficiently large sample, the effect should be negligible in a first approximation.

The network was trained on 5000 true and 10000 false tau candidates. The analysis was performed over the same sample, with 5000 additional false taus. The obtained performance curve is shown in figure 21 together with the corresponding curve for PDE-RS (from the same sample that has been used in the rest of the note). It is evident from these curves that PDE-RS is performing very close to the neural network. Taking into account that the neural network is overtrained, we conclude that the separation power would not be significantly improved by using this type of neural network.

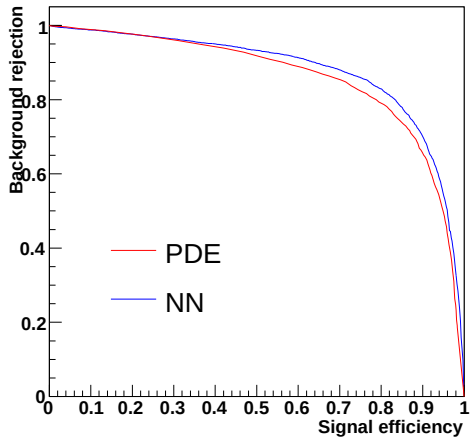

Figure 21: Performance of PDE-RS and a neural network on the SUSY sample. The efficiency and rejection in this case refers to the PDE-RS/NN part, not tau1P itself. Efficiency = 1 in this case simply means that the discriminator accepted all initial tau1P candidates. This of course leads to a correspondingly low background rejection (see also figure 9).

sparticle	mass [GeV]
χ_2^0	263.6
χ_1^0	136.9
$\tilde{\tau}_1$	146.5
$\tilde{\tau}_2$	257.0

Table 5: Important sparticle masses in the mSUGRA parameter point, calculated with ISAJET[18] 7.71.

3 Tau pair reconstruction in the mSUGRA stau coannihilation region

In this section we reconstruct the invariant mass of the tau pair in the decay chain $\chi_2^0 \rightarrow \tilde{\tau} + \tau; \tilde{\tau} \rightarrow \tau + \chi_1^0$ in the mSUGRA stau coannihilation region. The parameter point used is:

$m_0 = 70$ GeV, $m_{1/2} = 350$ GeV, $A_0 = 0, tan\beta = 10, sgn(\mu) = +$

The main reason for the high production rate of taus is the fact that the lightest stau is considerably lighter ($m_{\tilde{e}/\tilde{\mu}} - m_{\tilde{\tau}} \sim 100$ GeV) than the other sleptons, making tau decays preferred before others leptonic decay modes. The reason for the softness of the taus is that $\tilde{\tau}_1$ and $\tilde{\tau}_2$ are close to χ_1^0 and χ_2^0 in mass respectively, as seen from table 5. For our decay chain, illustrated by the Feynman diagram in figure 22, this always gives a soft tau, provided the system is not too boosted.

In a hadron collider experiment, the mass of the sparticles can be hard to determine, partly because of the missing energy due to the escaping neutralino, but also due to the

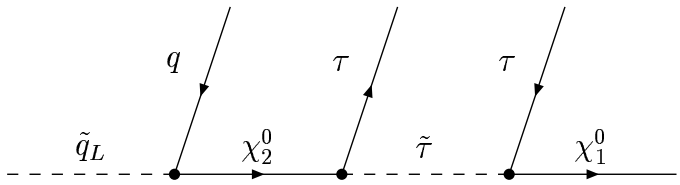

Figure 22: The cascade decay chain producing the tau pair in this study. One of the taus is always soft due to the $\tilde{\tau}$ / χ^0 mass ratio being close to one.

lack of knowledge of the total energy of the colliding partons. One can however extract information about masses by calculating the invariant mass of various combinations of particles from cascade decays. In this way limits on the underlying sparticle masses can be set [19].

In our particular decay chain, we measure the $\tau\tau$ invariant mass, given by equation 6. This should give a triangular shaped distribution, characteristic for decay to two leptons with an intermediate particle. The upper edge of such a distribution is given by equation 7. From this equation we find that decay via $\tilde{\tau}_1$ gives $m_{\tau\tau}^{max} = 77.8$ GeV, while decay via $\tilde{\tau}_2$ gives $m_{\tau\tau}^{max} = 49.2$ GeV. If we take $m_\tau = 0$, the expression reduces to eq. 8, and we get $m_{\tau\tau}^{max} = 78.0$ GeV and $m_{\tau\tau}^{max} = 49.6$ GeV respectively, showing that m_τ is not very important for the calculation of $m_{\tau\tau}^{max}$.

However, for the lower edge $m_{\tau\tau}^{min}$ (eq. 9, which reduces to zero in the $m_\tau = 0$ case, the effect is larger. For decay via $\tilde{\tau}_1$, $m_{\tau\tau}^{min} = 7.37$ GeV, and $m_{\tau\tau}^{min} = 7.05$ GeV for decay via $\tilde{\tau}_2$.

$$(m_{\tau\tau})^2 = 2m_\tau^2 + 2[E_1E_2 - |p_1||p_2|cos(\Delta\Omega)] \tag{6}$$

$$(m_{\tau\tau}^{max})^2 = 2m_\tau^2 + \frac{(m_{\tilde{\chi}_2^0}^2 - m_{\tilde{\tau}_x}^2 - m_\tau^2)(m_{\tilde{\tau}_x}^2 - m_{\tilde{\chi}_1^0}^2 + m_\tau^2)}{2m_{\tilde{\tau}_x}^2} + \frac{\sqrt{(m_{\tilde{\chi}_2^0}^2 - m_{\tilde{\tau}_x}^2 + m_\tau^2)^2 - 4m_\tau^2 m_{\tilde{\chi}_2^0}}\sqrt{(m_{\tilde{\tau}_x}^2 - m_{\tilde{\chi}_1^0}^2 + m_\tau^2)^2 - 4m_\tau^2 m_{\tilde{\chi}_1^0}}}{2m_{\tilde{\tau}_x}^2} \tag{7}$$

$$(m_{\tau\tau}^{max})^2 = \frac{(m_{\chi_2^0}^2 - m_{\tilde{\tau}_x}^2)(m_{\tilde{\tau}_x}^2 - m_{\chi_1^0}^2)}{m_{\tilde{\tau}_x}^2} \qquad \text{for } m_\tau = 0 \tag{8}$$

$$(m_{\tau\tau}^{min})^2 = 2m_\tau^2 + \frac{(m_{\tilde{\chi}_2^0}^2 - m_{\tilde{\tau}_x}^2 - m_\tau^2)(m_{\tilde{\tau}_x}^2 - m_{\tilde{\chi}_1^0}^2 + m_\tau^2)}{2m_{\tilde{\tau}_x}^2} - \frac{\sqrt{(m_{\tilde{\chi}_2^0}^2 - m_{\tilde{\tau}_x}^2 + m_\tau^2)^2 - 4m_\tau^2 m_{\tilde{\chi}_2^0}}\sqrt{(m_{\tilde{\tau}_x}^2 - m_{\tilde{\chi}_1^0}^2 + m_\tau^2)^2 - 4m_\tau^2 m_{\tilde{\chi}_1^0}}}{2m_{\tilde{\tau}_x}^2} \tag{9}$$

The analysed sample of 110000 events corresponds to an integrated luminosity of 16.3 fb^{-1} for a cross section of 6.76 pb.

3.1 Generator level distributions

We calculate the $m_{\tau\tau}$ distribution from generator level data, both for the tau energy and from the visible hadronic decay products. The result is shown in figure 23.

The upper left plot shows $m_{\tau\tau}$ for the desired decay chain, together with $m_{\tau\tau}$ for opposite sign (OS) tau pairs and same sign (SS) tau pairs from other decays. The characteristic triangular shape is clearly seen, and one can also notice the second endpoint at 50 GeV due to decay via $\tilde{\tau}_2$, discussed in the previous section.

Around 118 GeV, a very sharp additional peak is observed in the "other OS" distribution, coming from the decay of a Higgs boson to an OS pair. Another peak can be seen around 90 GeV, from $Z \to \tau\tau$, less pronounced due to the larger width of the Z. However, events with these decays are relatively rare, so we can safely ignore the contribution from these in our analysis.

The upper right plot shows the corresponding distribution for the hadronic decay products of the tau pairs.

The left plot in the lower row shows $m_{\tau\tau}$ for all tau pairs, for all OS pairs, and for all SS pairs. The triangular shape is no longer clear in this plot, but the endpoint is still intact.

On the right hand side, we see the corresponding distribution for hadronic decay products. This OS distribution is what we can expect to see in our reconstructed data, since we are unable to further select the tau pairs from the decay chain.

One could try to further improve on the signal by subtracting the SS distribution from the OS distribution (OS-SS in the figure). SS leptons do in most cases not belong to the same decay chain, so their combination should be random. We should therefore have an equal OS contribution from this effect. However, the "other OS" distribution in figure 23 is clearly larger than that of SS, most likely due to OS pairs from other sparticle decays. Thus we do not gain much background rejection, and as the OS-SS approach is also demanding on statistics, we will not use this in our following analysis of reconstructed data.

To estimate the endpoint given by eq. 8, we perform a linear fit to the OS $m_{\tau\tau}$ distribution in the range 40 -70 GeV, shown in figure 24. We define the endpoint as the point where the fit crosses the x axis. The endpoint of the fit is 75.8 ± 1.1 GeV, while the slope is $(-3.23 \pm 0.203) \times 10^{-3}$ GeV^{-1}. The fit was performed on a normalized distribution in order to be able to compare with distributions with different number of entries.

3.2 Reconstructed distributions

We now move to the reconstructed $m_{\tau\tau}$ distributions. The results are shown in figure 25 and 26 in terms of OS and SS distributions. As the distributions are selection dependent, we present plots for different likelihood and PDE cuts for both algorithms. The OS pair reconstruction efficiency and statistical significance corresponding to the plots are given for tauRec and tau1P in table 6. For each OS distribution, we perform the same linear fit as we did for the truth distribution in figure 24. The obtained fit parameters are shown in figure 27.

The pair reconstruction efficiency is higher for tau1P than for tauRec. This is mainly due to the higher cut on E_T^{seed} for tauRec, where the low energy part of the pair often will be rejected.

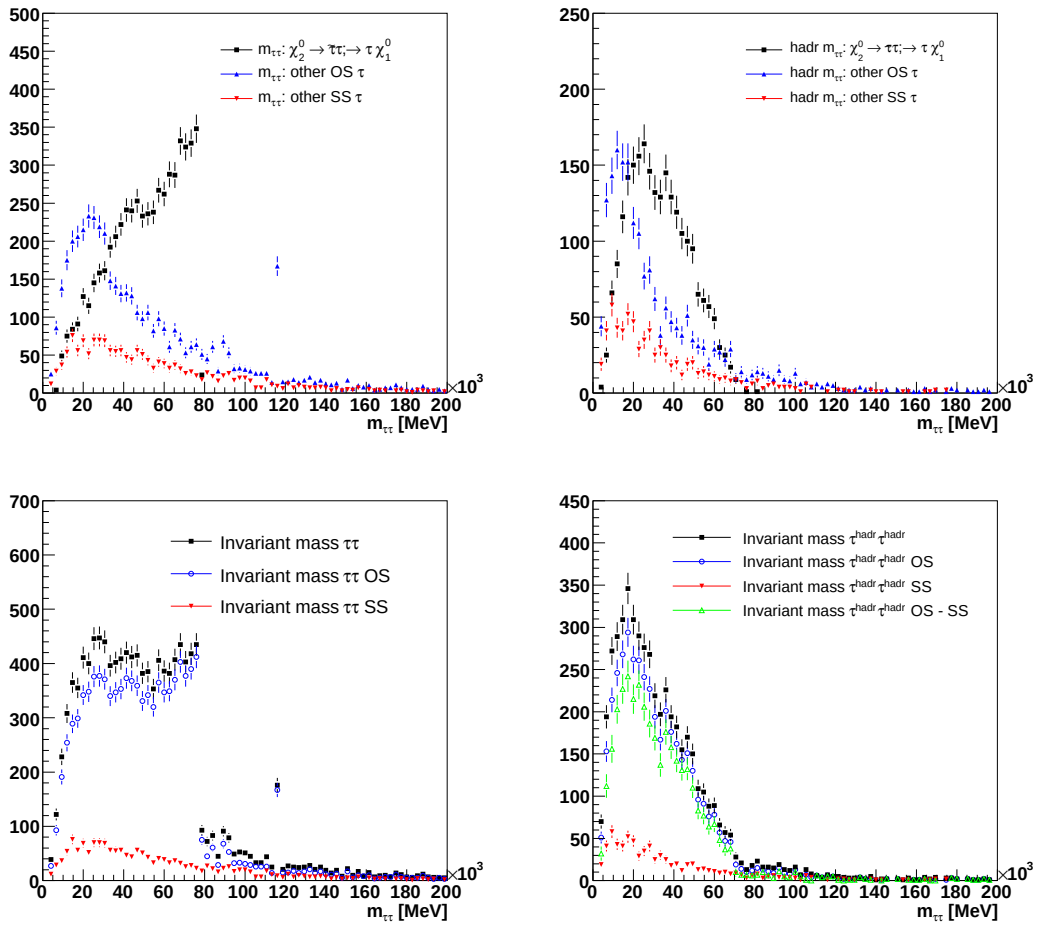

Figure 23: Invariant mass $m_{\tau\tau}$ for tau pairs on generator level. In the upper left plot, we see the distribution for the studied decay chain together with other OS and SS pairs. In the lower left plot we see the distribution for all pairs. The right hand plots shows the corresponding distributions for the invariant mass from hadronic decay products. The OS distribution in the lower right plot is what we can expect to observe in the detector.

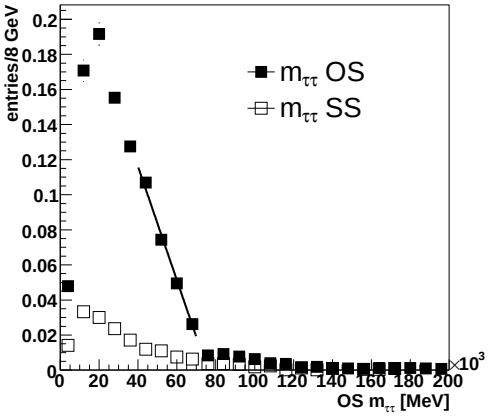

Figure 24: Normalized $m_{\tau\tau}$ OS and SS distribution with linear fit in range 40 - 70 GeV. The invariant mass is calculated from the hadronic decay products of the taus.

We observe that the fit parameters in figure 27 stay stable and close to the expected MC results also for loose PDE cuts. This indicates that our background is very similar to the signal we want to reconstruct. Looking at figures 25 and 26 we see that the SS and OS distributions are almost equal for the loose PDE cuts. But from figure 24, we know that the SS distribution should be much smaller than the OS distribution. This indicates that what we see for low PDE cuts in figures 25 and 26 is background in the form of mistagged jets. This contribution should be the same for both OS and SS, and dominates for the loose PDE cuts.

As we tighten the cuts, we see that the SS distribution falls off, and the distributions resembles more the MC distributions in figure 24. However, the fit parameters remain quite stable, since the shape of the OS mistag background is similar to our real signal.

Still, the falloff of the SS distribution is a sign that we are rejecting the false taus and are left with a larger fraction of the true distribution. This is also supported by the increasing statistical significance given in table 6.

In the fits, there is a general overestimation of the endpoint. This is most likely due to the less steep OS background, which shifts the endpoint towards higher mass. Another factor might be that tau1P overestimates E_T with up to 6% at low energies while underestimating with 2% at higher energies (see sec. 2.6). These E_T dependent shifts, as well as the error from the E_T and directional resolution, would have to be taken into account for calculation of the invariant mass in a full analysis.

In the previous section we observed that the background from true SS pairs was small compared to the true OS background. From this, we concluded that OS-SS subtraction would not be efficient for reducing the *true* OS background. However, the background of *false* OS pairs should be similar to that of false SS pairs. We can therefore assume that the false component of the OS distribution falls off in the same way as the SS contribution, which mainly consists of false pairs for low PDE cuts. This means that OS/SS subtraction could again be used, this time for rejecting the *false* OS background. However, our limited statistics still prevents us from using this technique.

Likelihood cut	Efficiency	$S/\sqrt{B}$
-10.0	$3.3 \pm 0.3\%$	2.4
-5.0	$3.2 \pm 0.3\%$	3.2
0.0	$2.2 \pm 0.2\%$	6.0
2.0	$1.9 \pm 0.2\%$	8.1
4.0	$1.4 \pm 0.2\%$	9.1
6.0	$0.9 \pm 0.1\%$	9.8

PDE-RS cut	Efficiency	$S/\sqrt{B}$
0.0	$7.2 \pm 0.4\%$	7.7
0.2	$6.3 \pm 0.4\%$	11.7
0.3	$5.9 \pm 0.4\%$	13.4
0.4	$5.6 \pm 0.4\%$	15.5
0.5	$4.9 \pm 0.3\%$	19.2
0.7	$2.9 \pm 0.3\%$	17.5

Table 6: Tau pair reconstruction efficiency and signal significance in SUSY sample for tauRec (left) and tau1P (right). S is true OS pairs, while B is false OS pairs.

For tauRec, the distribution is shifted higher in mass, mainly explained by the higher seed cutoff. This leads to a failure in performing the linear fit, but we observe that the SS distribution also here falls off with the likelihood cut. For likelihood cuts > 0, we observe what looks like a second peak in the distribution, around 100 GeV. This is actually an artifact from the background, a convolution of the rejection rate seen in figure 3 with the invariant mass from mistagging of jets. The lower peak at 50 GeV is the real $m_{\tau\tau}$ distribution.

3.3 Backgrounds to this channel

Since the aim of this analysis is not a full study of the parameter point used, but rather to evaluate the performance of the tau reconstruction algorithms in this scenario, a full background analysis is not performed. The background process from SUSY itself are included in the sample, as has already been shown in figure 23.

If one aimed to do a full analysis, both trigger and SUSY cuts[1] would have to be passed. The major background passing these cuts are $t\bar{t}$ production. Also, the sought after kinematical edge is very close to the Z peak, and thus quite sensitive to $Z \to \tau\tau$ decays. However, available Z production channels are not likely to pass the SUSY cuts, except from the SUSY related production itself, already included in this sample.

4 Conclusions

We have evaluated the performance of two tau reconstruction algorithms, tauRec and tau1P, with focus on soft taus. It was shown that tauRec and tau1P have similar default performance, but putting the focus of our optimization effort on tau1P, we found that the performance could be increased for the soft part of the tau E_T spectrum. Requiring the leading track in tau1P to be completely isolated rather than isolated from qualified tracks improved the background rejection, while lowering the E_T^{cell} cut reclaimed close to 10% of previously rejected good candidates without introducing much additional background. It was also found that discrimination with a neural network was not able to improve significantly on the discrimination power of PDE-RS.

[1] Typical SUSY cuts are $E_T^{miss} > 100$ GeV, 1st and 2nd jet with $E_T > 100$ GeV, 3rd jet with $E_T > 50$GeV.

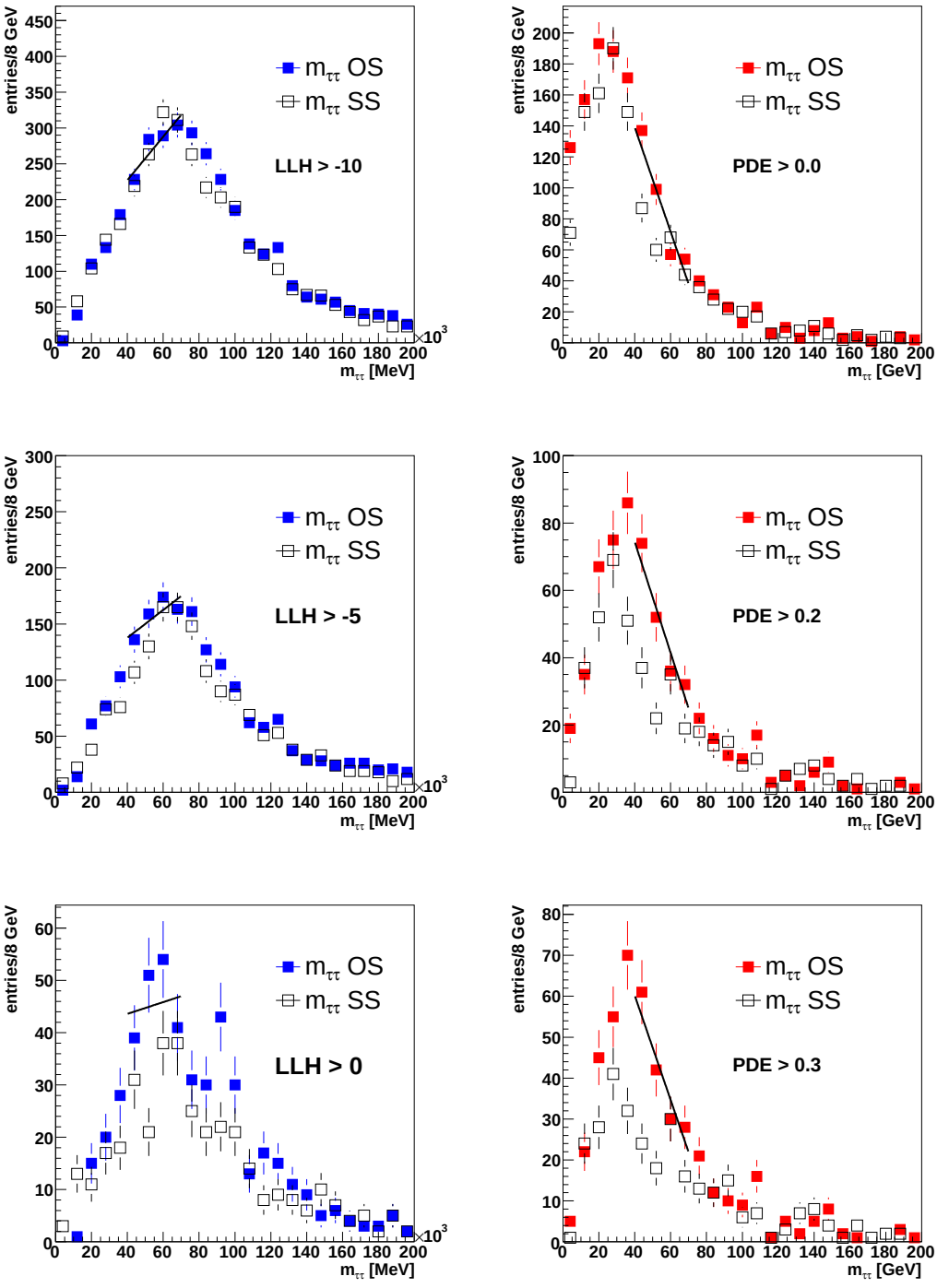

Figure 25: Reconstructed $m_{\tau\tau}$ from tauRec (left) and tau1P (right)

.

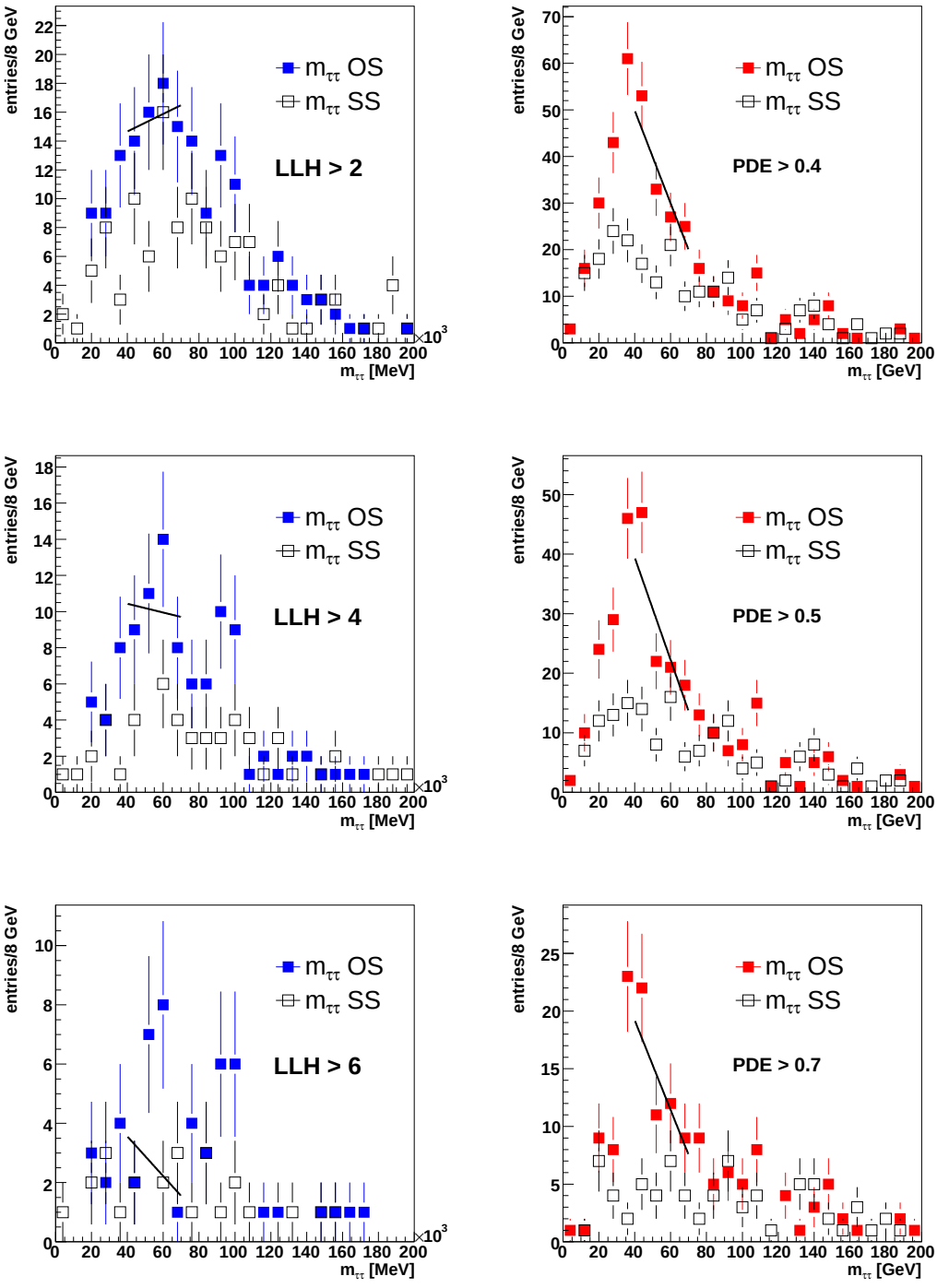

Figure 26: Reconstructed $m_{\tau\tau}$ from tauRec (left) and tau1P (right)

.

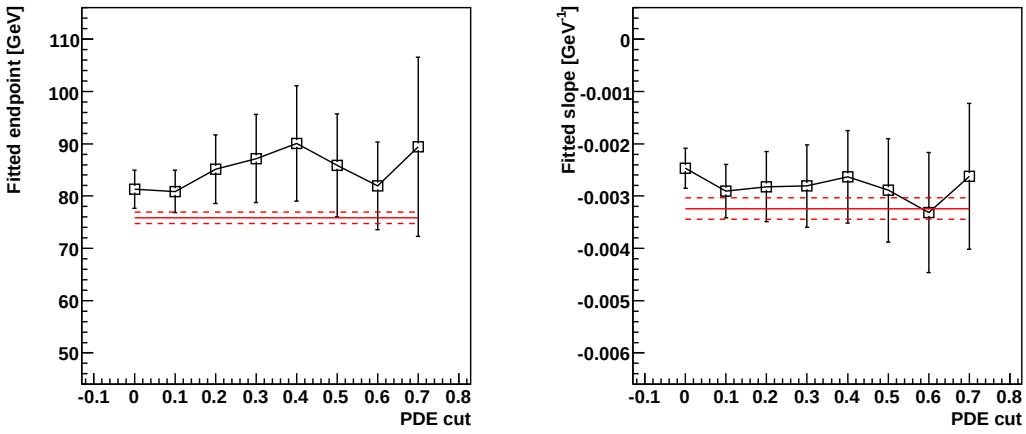

Figure 27: Fitted endpoint and slope as function of PDE cutoff for the tau1P distributions shown in figure 25 and 26. The red line shows the values from the fit to the true visible OS hadronic decay distribution in figure 24. The dashed lines indicate the uncertainty of the truth fit. In order to be independent of the number of entries in the different distributions, all fits have been performed on normalized histograms with equal binning.

It should be emphasised that some of the default cuts used for tauRec were not optimal, especially not the strip cut. This was low enough to pick up a negative contribution to strip width, rejecting a larger fraction of otherwise good candidates than tau1P.

The optimized tau1P and default tauRec were used to reconstruct the invariant mass of tau pairs in the chain $\chi_2^0 \to \tilde{\tau} + \tau; \tilde{\tau} \to \tau + \chi_1^0$, where reconstruction of the low E_T taus are crucial for reconstructing the tau pair. It was shown that the endpoint of the $m_{\tau\tau}$ distribution could be reconstructed with 16.3 fb^{-1} of data, using the optimized tau1P reconstruction.

However, both algorithms suffer from low statistics when reconstructing the invariant mass, resulting in large uncertainties in the fits, preventing us from using more statistically demanding methods like OS-SS subtraction. With higher statistics, one would also be able to use tighter cuts on both algorithms and in that way investigate to which degree energy and angular resolution plays a role in the endpoint determination.

Both tauRec and tau1P3P have undergone further development in the time after this study. TauRec now utilizes an improved likelihood method as well as a neural network for discrimination, while Tau1P3P/PDE-RS has been integrated into athena and extended to cover $|\eta| < 2.5$.

5 Acknowledgements

We would like to thank the authors of the two algorithms here studied, Michael Heldman (tauRec) and Elzbieta Richter-Was (tau1P3P) for valuable input during this study. We would also like to thank Frank E. Paige for sharing with us a large part of the SUSY data sample as ESDs. Finally we would like to thank Troels Petersen for providing the code

for the neural network and Are R. Raklev for help with kinematics.

This work has been performed within the framework of the ATLAS collaboration, and we have made use of tools which are the result of collaboration wide efforts.

References

[1] S. Martin, *A supersymmetry primer*, hep-ph/9709356

[2] M. Heldman, D. Cavalli, *An improved tau identification for the ATLAS experiment*, ATL-COM-PHYS-2006-10

[3] E. Richter-Was, L. Janyst, T. Szymocha, *The tau1P3P algorithm : implementation in Athena and performance with CSC data samples*, ATL-COM-PHYS-2006-029 (2006)

[4] J. Ellis, T. Falk, K. A. Olive, Phys.Lett. B444 (1998) 367-372 (hep-ph/9810360)

[5] S. Eidelmann et al., Physics Letters B592, 1 (2004)

[6] F. Mandl, G. Shaw, *Quantum Field Theory*, John Wiley and Sons Ltd 1984, ISBN 0-471-94186-7

[7] D. N. Spergel et al., Astrophys J. Suppl 148 (2003) 175 (astro-ph/0302209)

[8] M. Battaglia, I. Hinchliffe, D. Tovey, J.Phys. G30 (2004) R217-R244 (hep-ph/0406147)

[9] G. Corcella, I.G. Knowles, G. Marchesini, S. Moretti, K. Odagiri, P. Richardson, M.H. Seymour and B.R. Webber, JHEP 0101 (2001) 010 [hep-ph/0011363]; hep-ph/0210213

[10] T. Sjostrand, P. Eden, C. Friberg, L. Lonnblad, G. Miu, S. Mrenna and E. Norrbin, Computer Phys. Commun. 135 (2001) 238 (LU TP 00-30, hep-ph/0010017)

[11] Frank E. Paige, S. Padhi,
http://atlas.web.cern.ch/Atlas/GROUPS/PHYSICS/JETS/romeh1stylejetcal.pdf
(not the same version as used in this study, but explains the principles).

[12] Atlas Computing Technical Design Report, ATLAS TDR-017, CERN-LHCC-2005-022 (2005)

[13] Froidevaux, D.; Nevski, P.; Richter-Was, E. *Energy flow studies with hadronic tau-decays using DC1 data samples*, ATL-COM-PHYS-2005-024 (2005)

[14] J. M. Butterworth, J. P. Couchman, B. E. Cox, B. M. Waugh, Comp. Phys. Comm. vol 153/1 85-96 (2003)

[15] T. Carli, B. Koblitz, NIM A501 (2003) 576-588.

[16] Atlas InnerDetector Technical Design Report, ATLAS TDR-4, CERN/LHCC/97-16, ISBN 92-9083-102-2

[17] T. Pedersen, *http://www.nbi.dk/ petersen/NeuralNet/neuralnet.html*

[18] H. Baer, F. E. Paige, S. D. Protopopescu and X. Tata, *"ISAJET 7.48:A Monte Carlo event generator for p p, anti-p p, and e+ e- reactions*" (hep-ph/0001086)

[19] B. K. Gjelsten, D. J. Miller, P. Osland, JHEP 0412 (2004) 003 (hep/ph-0410303)